Journal of Non-Crystalline Solids 425 (2015) 1–10

Contents lists available at ScienceDirect

Journal of Non-Crystalline Solids

journal homepage: www.elsevier.com/ locate/ jnoncrysol

Sol–gel hybrid coatings with strontium-doped 45S5 glass particles for enhancing the performance of stainless steel implants: Electrochemical, bioactive and *in vivo* response

Sheila Omar [a], Felix Repp [b], Paula Mariela Desimone [a], Richard Weinkamer [b], Wolfgang Wagermaier [b], Silvia Ceré [a], Josefina Ballarre [a,*]

[a] INTEMA, National Research Council (CONICET), Universidad Nacional de Mar del Plata (UNMdP), Juan B. Justo 4302, Mar del Plata, Argentina
[b] Max Planck Institute of Colloids and Interfaces, Department of Biomaterials, 14476 Potsdam, Germany

ARTICLE INFO

Article history:
Received 19 February 2015
Received in revised form 16 April 2015
Accepted 16 May 2015
Available online xxxx

Keywords:
Stainless steel;
Coatings;
Strontium;
Bioactivity;
Corrosion;
Osseointegration

ABSTRACT

The protection of stainless-steel implants by applying a hybrid organic–inorganic coating generates a barrier for ion migration and a potential holder for functional particles. Chemical composition of bioactive silicate-glasses (BG) can be varied to tailor their rate of dissolution in the biological environment. The substitution of calcium by strontium (Sr) generates a locally-controlled release of Sr-ions to the media. Strontium is known to reduce bone resorption and stimulate bone formation.

This work presents coatings made by sol–gel method containing tetraethoxysilane, methyl-triethoxysilane and silica nanoparticles as precursors, and functionalized either with BG or Sr-substituted BG particles onto surgical grade stainless steel. The coated implants were tested *in vitro* for corrosion resistance and bioactivity, and *in vivo* to analyze bone formation.

The applied coating system provided an excellent protection to aggressive fluids, even after 30 days of immersion. The presence of hydroxyapatite is shown as a first evidence of bioactivity. The evaluation of *in vivo* tests in Wistar–Hokkaido rat femur 4 or 8 weeks after the implantation showed slight differences in the thickness of newly formed bone measured by ESEM, and remarkable changes in bone quality characterized with Raman microscopy. The *in vivo* response of the coatings containing Sr-substituted bioglass is better at early times of implantation as regards the bone morphology and quality making this functionalized coatings a very promising option for implant protection and bone regeneration.

1. Introduction

The interaction between a permanent dental and orthopedic prosthesis with living tissue is the motivation for many studies. In Latin America there are several economic considerations that impede people the access to first class materials for intracorporeal permanent implants, routinely used in developed countries. For this reason, there is still a strong demand for surgical grade stainless steel.

The low grip, loosening or detachment by infection, wrong surgical technique or corrosion of structural materials used as bone substitutes are some of the most common causes of failure which necessitates the removal of the implant [1,2]. As the surface plays a key role in the interaction between implant and the existing tissue, conditioning the success or failure of the implant; this issue is the main concern of the present study.

The improving of materials' surfaces can be achieved either by chemical, electrochemical or thermal treatment, or by applying compact adherent coatings. Organic–inorganic hybrid materials have drawn researchers' attention due to their unusual combination of physical and chemical properties [3,4]. A family of materials with great future potential is derived from the hydrolytic condensation products of functionalized alkoxides, either pure or enriched with tetraethoxysilane (TEOS) [5,6]. The final hybrid material is obtained by crosslinking the organic groups by polymerization and/or by condensation of Si–OH groups (silanols). Coatings made by the sol–gel method have many advantages compared with other deposition techniques: good adhesion, easy application, no drying problems, low temperatures of densification, and the possibility to functionalize films by adding particles and/or by the

Abbreviations: BG, bioglass 45S5; BGSr, bioglass 45S5 containing strontium; BSE, back scattering electron; CPE, constant phase element; Ecorr, corrosion potential; EIS, electrochemical impedance spectroscopy; ESEM, environmental scanning electron microscopy; HA, HCA, hydroxyapatite, hydroxyl carbonated apatite; MTES, methyl triethoxysilane; PMMA, poly methyl methacrylate; SBF, simulated body fluid; SEM, scanning electron microscopy; T-BG, TEOS–MTES–SiO_2 coating with bioglass particles; T-BGSr, TEOS–MTES–SiO_2 coating with bioglass particles partially substituted with strontium; TEOS, tetraethoxysilane; TMS, TEOS–MTES–SiO_2 system coating.

* Corresponding author at: Material's Science and Technology Research Institute (INTEMA), UNMdP-CONICET, Juan B. Justo 4302, B7608FDQ Mar del Plata, Argentina.
E-mail address: jballarre@fi.mdp.edu.ar (J. Ballarre).

http://dx.doi.org/10.1016/j.jnoncrysol.2015.05.024
0022-3093/

presence of organic groups [7–10]. Bioceramics are produced in a variety of forms and phases and have different functions, where the most common is as material for filling defects [11,12]. Additionally, bioceramics can be used as coatings on substrates or as a second phase in composites. In these cases the properties of the bioceramics help in enhancing both the mechanical and biochemical properties [13–15].

Thanks to its positive effects on bone biology, the incorporation of strontium (Sr) in ceramic and calcium phosphate cements has been a topic of great interest in the last decade [16–19]. Strontium-containing agents have been shown to inhibit bone resorption by osteoclasts and promoting osteoblast replication and bone formation [20]. It has been demonstrated that calcium phosphate ceramics containing Sr can be considered as bone-precursors since they promote adhesion and osteoblast proliferation, showing no deterioration and slow degradation with time caused by cell adhesion, extracellular matrix formation and mineralization *in vitro* [21]. Several studies showed that hydroxyapatite bone cements containing Sr promote osteoblast adhesion and mineralization *in vitro* [22] as well as growth and bone integration *in vivo* [23–26]. While the bioactive glasses or bioactive glass-ceramics have been extensively studied as a way to stimulate bone response, the effects of a modification with Sr are largely unexplored.

Carbonate concentration in calcified tissues varies with the type of tissue (enamel, dentine, bone), maturity, crystallinity, and the bone structural features such as history of fracture. Vibrational spectroscopy (infrared and Raman) is an ideal method for analyzing mineral structure since it is sensitive to changes in crystallinity and molecular substitution. The ratio of the carbonate band to the phosphate band provides the degree of carbonate substitution in the lattice structure of the apatite [27]. Mineral crystallinity is also a parameter of mineral maturation. Changes in crystal size and in lattice perfection are reflected in crystallinity obtained by Raman or infrared spectroscopy.

The aim of the present work is to analyze the performance of two coatings applied onto stainless steel implants in view of their bone ingrowth. We investigate hybrid coatings obtained by the sol–gel technique containing bioactive glass particles doped with Sr applied on surgical grade stainless steel for implantation purposes. The coated system is thought to have better anti-corrosive protective behavior than the bare material, as well as a bioactive response as evidenced by apatite deposition when immersed in simulated body fluid (SBF). The formation of new bone around the functionalized coatings tested *in vivo* should be further stimulated by the addition of strontium when compared to bone formation with only bioglass 45S5 particles.

2. Materials and methods

2.1. Substrates

Stainless steel AISI 316L (Atlantic Stainless Co. Inc., Massachusetts, USA) in plates and nail-like shape (plates $3 \times 2 \times 0.2$ cm^3, nails 1.5 cm long 0.12 cm diameter) were used as substrates (named SS samples). The composition of the steel was: C 0.03% max, Mn 2% max, Si 1% max, P 0.045% max, S 0.03% max, Ni 10–14%, Cr 16–18%, Mo 2–3%, and balance Fe. The samples were degreased, washed with distilled water and rinsed in ethanol before coating.

2.2. Sol–gel solution

Hybrid organic–inorganic sols were prepared with a silicon alkoxide, tetraethoxysilane (TEOS, 99% ABCR), a silicon alkyl alkoxide, methyltriethoxysilane (MTES, 98% ABCR) and colloidal silica suspended in water (SiO_2, LUDOX 40 wt.%, Dow). The molar ratio of the alkoxide was kept constant (TEOS/MTES = 40/60) and the addition of colloidal silica was 10% in moles with respect to the total amount of SiO_2. The final silica concentration was for both sols 4.16 mol/L and the water amount was kept stoichiometric.

2.3. Bioactive particles, suspension and coatings

Two kinds of bioactive particles were made: BG: 45S5 Bioglass® and BGSr: 45S5 glass where calcium was partially substituted with 2 mol% of strontium [28] (Table 1). BG and BGSr were milled in planetary mill equipment (Fritsch Pulverisette, Germany) and screened with a Tyler screen to obtain particles with a diameter smaller than 20 μm. A 5–10% wt/wt of particles were added to the sol, then they were stirred by a high shear mixer in a rotor–stator agitator (Ultra-Turrax T-25 IKA, China) within 6 min. Phosphoric ester and citric acid in low concentration (less than 1 wt.% of bioactive particles) were added as dispersants in the bioglass particles containing suspensions. Ester works as surfactant that adsorbs on the surface of the particles, creating an electrostatic repulsion between the particles and avoiding segregation [29].

Double-layer coatings were applied on the substrates in two steps. The first layer prepared with TEOS–MTES–SiO_2 (called TMS) sol was obtained at room temperature by dip-coating at a withdrawal rate of 20 cm·min^{-1}, dried at room temperature for 0.5 h, and then heat treated for 0.5 h at 450 °C in an electric furnace. The second layer of TMS containing either BG or BGSr particles was applied on top of the first layer at 12 cm·min^{-1} withdrawal rate and the same thermal treatment than for the coatings without the particles.

Four different samples were used and analyzed in this work: SS, stainless steel; TMS, double layer of TEOS–MTES–colloidal SiO_2; T-BG: first layer of TMS and upper layer of TMS with bioactive BG particles; and T-BGSr: first layer of TMS and upper layer of TMS with BGSr particles.

2.4. In vitro coating characterization

The coated systems were analyzed *in vitro* by immersion in a solution that simulates the inorganic concentration of ions in the human plasma. The objective is to detect the presence of hydroxyapatite and to simulate long exposition to corrosive fluids.

A simulated body fluid (SBF) solution was used as electrolyte in all the experiments. SBF was prepared with the following chemical compositions [30]: NaCl (8.053 g·l^{-1}), KCl (0.224 g·l^{-1}), $CaCl_2$ (0.278 g·l^{-1}), $MgCl_2 \cdot 6H_2O$ (0.305 g·l^{-1}), K_2HPO_4 (0.174 g·l^{-1}), $NaHCO_3$ (0.353 g·l^{-1}), and $(CH_2OH)_3\,CNH_2$ (6.057 g·l^{-1}). Concentrated hydrochloric acid (HCl) was added to adjust the pH to 7.25 ± 0.05. The samples were immersed in SBF for 30 days, and sealed at 37 °C in a sterilized furnace until the tests were done.

The thickness of the coatings was measured with a profilometer KLA Tencor (Alpha-Step D-100, US) for the TMS system. A "step" or the end of the layer was measured comparing with the substrate surface, thereby avoiding the so-called border effects of the coatings' deposition.

Particle distribution, coating integrity and homogeneity were examined by scanning electronic microscopy (SEM) with a JEOL JSM-6460LV (Japan) equipment prior to immersion and after 30 days of immersion in SBF. In order to analyze *in vitro* bioactivity, micro-Raman assays were conducted on previously immersed samples in SBF for 30 days at 37 °C using an inVia Reflex confocal (Renishaw RM2000, UK) with a 514 nm wavelength laser, at 100% intensity in a window from 400 to 1300 cm^{-1}, and 50 second exposition per spectrum.

Table 1
Composition in mol for the bioactive glasses Bioglass®45S5 (BG) and Sr-substituted 45S5 (BGSr).

(In mol)	SiO_2	Na_2O	CaO	SrO	P_2O_5
BG	46.13	24.35	26.91	0	2.6
BGSr	46.13	24.35	24.89	2.02	2.6

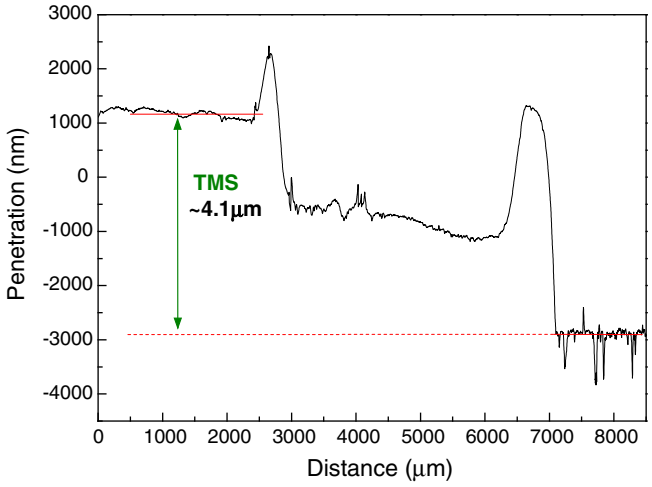

Fig. 1. Profilometer curve of a stainless steel sample coated with two layers of TMS coating. , shown at the right of the curve is the substrate surface roughness.

2.5. Electrochemical analysis

Electrochemical assays were carried out in a GAMRY Ref 600 electrochemical unit (Gamry, USA) with a conventional three electrode cell. The reference electrode was a saturated calomel electrode (SCE, Radiometer, Copenhagen), a platinum wire as a counter electrode and the stainless steel, either bare or coated, as working electrode. SBF was used throughout the experiments.

Potentiodynamic polarization curves were conducted from the corrosion potential (Ecorr) to 1 V and backwards, or up to a maximum current density of 0.001 $A \cdot cm^{-2}$ at a sweep rate of 0.002 $V \cdot s^{-1}$.

Electrochemical impedance spectroscopy (EIS) tests were registered at the Ecorr with an amplitude of 0.005 V rms, (root mean square) sweeping frequencies from 20,000 to 0.02 Hz. Impedance data fitting was performed using Zplot software [31].

The interpretation of the experimental data of the complex impedance spectra with a physical corrosion process model of the metal/coating interface, can lead to a better comprehension of the degradation mechanisms involved. The use of equivalent circuits allows assigning electric elements to different components of the system under study. Impedance spectra can be, therefore, associated with an electric response fitting the values in the curves using different equivalent electric circuits. In this work Constant Phase Elements (CPE) instead of capacitances were used when phase angle was different from −90°. The impedance for the CPE, Z_{CPE}, element can be written as [32]

$$Z_{CPE} = \frac{1}{Q(j\omega)^{\alpha}}, \tag{1}$$

where Q (pseudocapacitance) and α are the CPE parameters, independent of frequency, j is the current density and ω the frequency.

The CPE is generally attributed to distributed surface reactivity, surface inhomogeneity, roughness or fractal geometry, electrode porosity, and to current and potential distributions associated with electrode geometry [33]. It is clear that the CPE parameter Q cannot represent the capacitance when $\alpha < 1$ in Eq. (1). Q can be related to the effective capacity (*Ceff*) of the analyzed coating, applying a surface distribution of the elements, which leads to the result [34]

$$Ceff = Q^{1/\alpha}\left(\frac{\mathrm{Rsol}\cdot\mathrm{Rcoat}}{\mathrm{Rsol}+\mathrm{Rcoat}}\right)^{\frac{1-\alpha}{\alpha}} \tag{3}$$

Rsol is the solution or medium resistance and Rcoat is the coating resistance. In the limit that Rcoat becomes infinitely large, Eq. (3) becomes:

$$Ceff = Q^{1/\alpha}\mathrm{Rsol}^{\frac{1-\alpha}{\alpha}} \tag{4}$$

which is equivalent to the equation presented by Brug et al. [35] for a blocking electrode. In the present work *Ceff* was calculated for the high frequency CPE of the electric circuits, which represents the pseudocapacitance of the coating. *Ceff* can be related to the thickness of the coating, d, the dielectric constant of the coating ε and the exposed area, A, as

$$Ceff = \frac{\varepsilon\varepsilon_0 A}{d} \tag{5}$$

with ε_0 the free space permittivity.

2.6. In vivo implantation

In vivo experiments were conducted with 6 Wistar–Hokkaido (WKAH/Hok) male adult rats (weight 350 ± 50 g), according to the rules of ethical committee of the National University of Mar del Plata (Interdisciplinary Committee, April 2005/October 2010), taking care of surgical procedures, pain control, standards of living and appropriated death. Coated and uncoated wires were sterilized in autoclave for 20 min at 121 °C. Rats were anesthetized with Ketamine and Xilacine (100 mg/kg, 10 mg/kg) according to their weight. The region of surgery surface was cleaned with antiseptic soap. The animals were placed in a supine position and the implantation site was exposed. A region of around 0.5 cm diameter was scraped in the femur plateau and a hole was drilled using a hand drill of 0.125 cm diameter at low speed. The coated and uncoated wire implants (used as controls) were placed by press fit into the medullary canal of the femur. The animals were sacrificed after 4 and 8 weeks with an overdose of intraperitoneal sodic thiopental (120 mg/kg) with a previous anesthesia as described

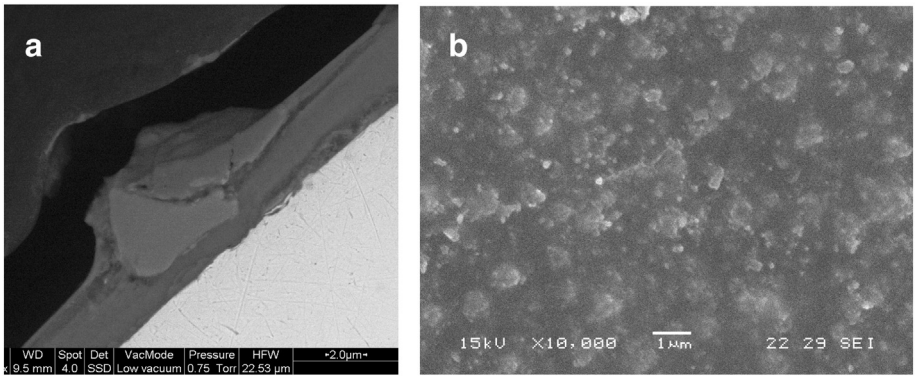

Fig. 2. Back scattering ESEM images of the T-BG coatings: (a) cross section and (b) surface.

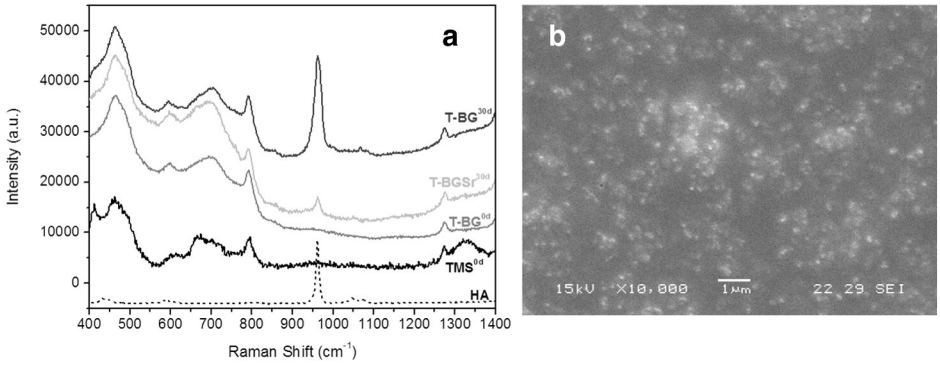

Fig. 3. (a) Raman spectra of the analyzed coatings (TMS, T-BG and T-BGSr) with immersion and without immersion in SBF. The hydroxyapatite spectrum (HA) is shown as a reference; (b) SEM image of the T-BG surface after 30 days of immersion in simulated body fluid.

above and the femur with implant was retrieved. Conventional X-ray radiographs were taken before retrieving the samples for control of the correct position of the implant into the bone marrow cavity.

The retrieved samples were cleaned from surrounding soft tissues and fixed in neutral 10 wt.% formaldehyde for at least 24 h. Then they were dehydrated in a series of alcohol–water mixture followed by a methacrylate solution and finally embedded in poly-methyl methacrylate (PMMA) solution and polymerized for 5 days at 32 °C. The PMMA embedded blocks were cut into thin slices with a low speed diamond blade saw (Buehler GmbH) cooled with water and polished to obtain 100 μm thick sections.

2.7. Image analysis of in vivo samples

The surface morphology of the implant–bone interface was observed with environmental scanning electron microscopy (ESEM, Quanta 600 FEG) in low vacuum using back scattered electron (BSE) detector operated at low voltages. The BSE images reveal the mineralized tissue regions, but do not visualize the unmineralized soft tissue layer formed around the implant. Measurements of the thickness of the newly formed bone were done in an automated manner using a custom-made program written in Python [36].

Segmentation of the image was done using a global threshold to define the implant, and using an adaptive threshold to segment the bone. The image was then transformed into a polar coordinate system with the origin of the coordinate system being the center of the implant. Using azimuthal sectors of 6° for each sector the average thickness of the newly formed bone, as well as the thickness of the gap between implant and bone was determined for each sample. The width of the peak distribution of these average thicknesses is used to describe the uncertainty of the measurement. Regions which the implant is close to the cortex, and therefore susceptible for imaging artifacts, were excluded from the analysis.

The quality of the formed bone around the implanted samples was analyzed by Micro-Raman Spectroscopy, as was detailed in previous works [37,38]. The equipment used was an inVia spectrometer (Renishaw, UK) system equipped with charge-coupled device (CCD) detector of 1040 × 256 pixels and coupled to a Leica microscope (DM-2500 model) (50×, 0.75 NA) with a computer-controlled x–y–z stage. A diode laser line (785 nm) was used as excitation source in combination with a grating of 1200 grooves/mm. The laser power was kept below 10% to avoid sample damage, employing one 10-sec acquisition for each data point. The spectral resolution was 4 cm^{-1}, and the spectra were taken from 300 to 1800 cm^{-1}. In each sample, a region near the implant with newly formed tissue was studied. A matrix of 4 × 5 points/spectra where done, which was averaged and statistically analyzed.

Background fluorescence in the spectra was subtracted by a modified polynomial fitting algorithm. Band intensities were recorded for amide I (1650 cm^{-1}), amide III (1245 cm^{-1}), CH_2 wag (1450 cm^{-1}) B-type carbonate (1071 cm^{-1}), $\nu1$ phosphate (960 cm^{-1}), and $\nu2$ phosphate (430 cm^{-1}) using a custom-made Matlab program. The mineral to matrix ratio was calculated based on the intensity ratio of the $\nu1$ phosphate band to either the amide I or CH_2 wag, and the $\nu2$ phosphate band to amide III band intensity. The carbonate substitution was calculated by the ratio $CO_3^{2-}/\nu1$ phosphate, and the degree of crystallinity was determined as the inverse of the width of the phosphate symmetric-stretch band ($\nu1$ PO_4^{3-} at 960 cm^{-1}) at the half maximum intensity value ($FWHM^{-1}$) [39].

3. Results

3.1. Coating characterization

The homogeneity and thickness of the system is shown in Fig. 1. The TMS coatings presented good homogeneity and no presence of flaws.

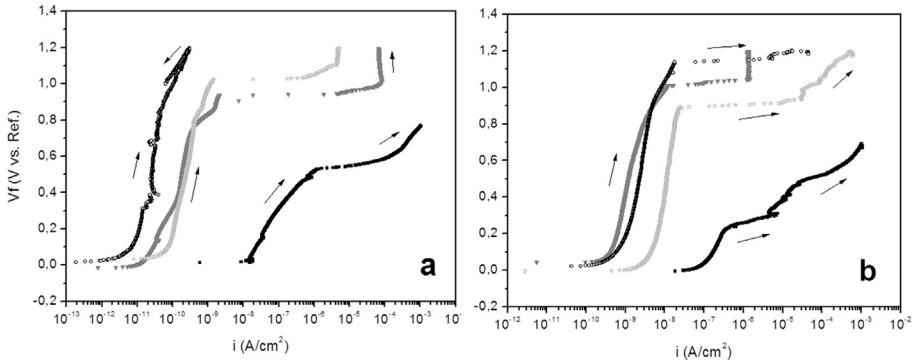

Fig. 4. Potentiodynamic polarization curves for all conditions of study (SS ■, TMS ○, T-BG ▼ and T-BGSr ⋆ coatings) (a) after 1 h of immersion, and (b) after 30 days in SBF at 37 °C.

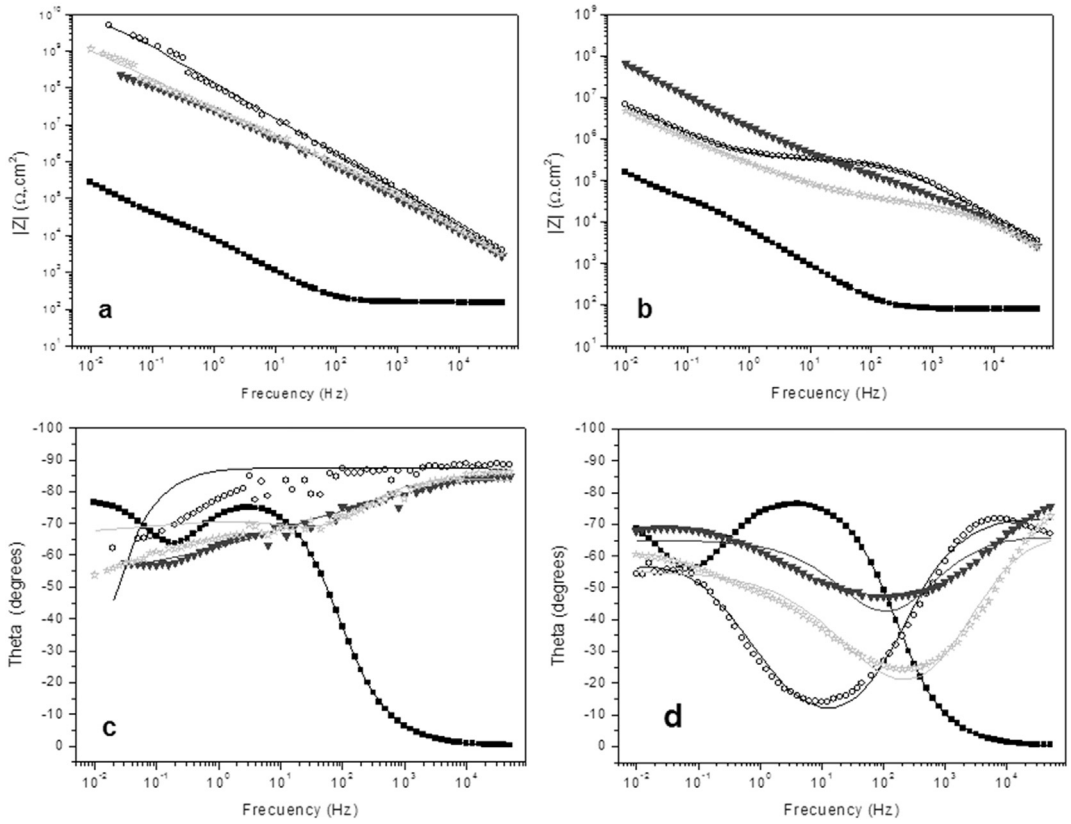

Fig. 5. Electrochemical Impedance Spectroscopy Bode representation plots for all studied conditions: SS ■ bare metal, TMS ○ coating, T-BG ▼ coating and T-BGSr ⋆ coating after 1 h of immersion (a and c) and after 30 days in SBF at 37 °C (b and d). The solid lines represent the result of the data fitting.

The main thickness of a single TMS coating is 2.1 +/− 0.4 μm, with no change after SBF immersion. The original stainless steel surface roughness appears at the right of the curve line, and the final roughness, at the left. In the figure the soft and continuous surface profile can be observed for the coating when compared with the bare steel. When the particles were added, some remained within the coating, while a fraction of them could be observed on the surface (Fig. 2a). The stirring, suspension and the aggregate of additives are a key issue for particle distribution. In both coatings studied only the fraction of particles with smaller diameter was suspended while the bigger ones precipitated (Fig. 2b).

3.2. In vitro HA deposition

With the aim of determining the ability of the coating to induce the formation of hydroxyapatite (HA) on the surface, Raman spectra were measured before and after the exposition to the simulated body fluid for 30 days (Fig. 3a). The spectrum of hydroxyapatite was used as a comparison. As it was expected, no presence of apatite related compound were found in the T-BG and T-BGSr samples before immersion, but also no presence of any bands related to the BG particles were found.

After 30 days of immersion the surface, which is still covered with the TMS coating, showed the same bands as in the samples without immersion, but in addition new bands could be observed and could be associated to some deposits on the surface (Fig. 3b). After immersion of the T-BG and T-BGSr samples in SBF, carbonated HA related bands that could be detected are: the typical 960 cm^{-1} band corresponding to PO_4^{3-} first vibration and an insight of a CO_3^{2-} vibration band (1070 cm^{-1}) [40].

3.3. Electrochemical coating integrity

Fig. 4 shows the behavior of the different studied systems by applying a raising potential from Ecorr and measuring the current density. The samples presented very low current density values, three decades lower than the bare steel, immediately after immersion (called samples after 1 h of immersion). Also no breakdown potential (E_{break}) was observed in the TMS coating, pointing out the integrity of the layers.

After 30 days of immersion, current densities of all the coated systems remained two orders of magnitude lower than the stainless steel, indicating that – even though there is a slight deterioration of the coatings due to particle release and dissolution – the coatings still remain protective when compared with the bare stainless steel. It is worth noting that in all the measured conditions, the E_{break} is more than 0.4 V higher for the coated samples than for the bare material, showing the stability of the film against localized corrosion [41,42].

Electrochemical impedance spectroscopy (EIS) tests on all bare and coated stainless steel samples were carried out after 1 h of immersion and after a 30 day immersion in SBF. Bode plots (impedance modulus *vs* frequency and phase angle *vs* frequency) are shown in Fig. 5.

All the coated systems presented in the early stages of immersion, a high total impedance, which can be read extrapolating at zero

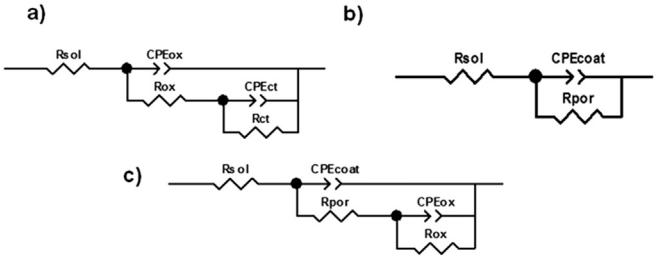

Fig. 6. Equivalent electric circuits employed to model the impedance data: (a) SS after 1 h of immersion and 30 days of immersion in SBF; (b) TMS after 1 h of immersion in SBF; and (c) TMS 30 days and T-BG and T-BGSr at the beginning of immersion and 30 days of immersion in SBF.

Table 2
Fitting parameters for the uncoated stainless steel samples using the equivalent circuit shown in Fig. 6(a).

	Rsol (Ω cm^2)	CPEox		Rox (Ω cm^2)	CPEct		Rct (Ω cm^2)	*Ceff* (F cm^{-2})	
		Q (Ω^{-1} cm^{-2} s$^{\alpha}$)	α		Q (Ω^{-1} cm^{-2} s$^{\alpha}$)	α		Mean	SD
SS									
0	43	8.04E−05	0.89	1.17E+04	7.97E−05	0.93	1.42E+06	1.08E−5	2.08E−06
30	76	2.82E−05	0.89	6.16E+04	5.04E−05	0.88	2.87E+06	1.60E−5	4.55E−06

frequency in the |Z| vs. Frequency plot. The total impedance of the coated systems is between 4 and 5 orders of magnitude higher compared with the bare metal. After 30 days of immersion the total impedance is still higher than the SS sample in all the cases, but shows a slight decrease for the TMS and the T-BGSr coating system.

The phase angle θ *vs* Frequency Bode plot of the samples after 1 h of immersion shows a very plane curve with a decreasing tendency without reaching the zero value at low frequencies for the TMS, T-BG and T-BGSr coatings. This could be related to a film with high integrity, with a capacitive behavior at high frequencies. After 30 days of immersion two time constants can be observed for the coated systems. A deterioration of all coatings can be noticed since the systems are loosening their capacitive behavior with a shift of the high frequency time constant.

The stainless steel samples at both times of immersion were fitted with an equivalent electric circuit with the solution resistance (Rsol) in series with a two capacitive–resistive elements in parallel, as can be seen in Fig. 6a. There is a one phase constant element, CPEox, representing the metal oxide and its resistance, Rox, and other leaking capacitor (CPEct) and a resistance (Rct) that represents the charge transference events at the metal surface. The fitted parameters are shown in Table 2. The *Ceff* was calculated according to Eq. (3). After 30 days of immersion of the bare material in SBF, the fitted parameters do not showed significative changes in the mean values. The *Ceff* remains around 1.5E–5F·cm^{-2}.

For modeling the TMS behavior at the beginning of immersion, a simple circuit with a Constant Phase Element (CPE) instead of a capacitor, and a resistance were used, where CPEcoat represents the leaking capacitor modeling the coating and Rpor representing the resistance of the electrolyte when entering into the pores of the coating (Fig. 6b).

After 30 days of immersion, the TMS coating suffers some degree of deterioration and the behavior or the system can be modeled with a two phase constant-resistances elements in parallel, as the bare stainless steel after 30 days of immersion. But in this circuit the second pair of CPEox in parallel to Rox, is related to the oxide of the metal (Fig. 6c).

For both times of immersion of the T-BG and T-BGSr coating systems, the experimental data were fitted with the same equivalent circuit used for the TMS coating after 30 days of immersion. Accordingly, Qcoat and Qct represent the pseudocapacitance of the CPEcoat and CPE charge transfer respectively. Rpor and Rct, represent the electrolyte into the pores and charge transfer resistance, respectively. In the case of the coated samples with particles for all times of immersion, the Rct is very large and tends to infinity, making all the current flow via the other path of the circuit, thereby acting as a partially blocked electrode. In these systems, a section of the surface covered by particles or deposits, acts as a blocked site assumed to be a perfect insulator [43]. The fitted electrochemical parameters are shown in Table 3. In all the cases, the standard deviation given in percentage was less than 15%.

In all the analyzed coated samples, the pseudocapacitance Q of the CPEcoat rises with immersion time, and the value of α decreases. The Rpor in TMS coating falls dramatically from $6.4 * 10^9$ to $3.1 * 10^5$ Ω cm^2 with time, but the total resistance increased by the Rox ($6.9 * 10^7$ Ω cm^2) presence. In T-BG and T-BGSr coating systems, there is a slight decrease in the Rpor after 30 days immersion in SBF. Also the value of the Q of the CPEox changes: it increases with time, showing a higher change for T-BGSr coatings. These results are consistent with the ones observed for the potentiodynamic curves, where the TMS suffers more deterioration due to the immersion than the other coated systems, being the T-BG system the more integer coating after the immersion. It is worth noting, however, that all the investigated systems showed better corrosion resistance than the bare SS in the immersion time under study.

3.4. Analysis of in vivo samples

Fig. 7(a, c) and (b, d) shows representative ESEM images of the T-BG and T-BGSr implants after 4 weeks of implantation in Wistar rat femurs. Newly grown bone tissue can be identified around the implant growing in contact with the bone marrow. The growth direction of lamellar bone tissue seems to be perpendicular to the longer axis of the nail-like implant. Images from all the samples had a similar morphology, but showed differences in the thickness and compactness of the newly grown bone. The evaluated thickness of the newly formed tissue around the implants 4 and 8 weeks after implantation is shown in Table 4.

After 8 weeks the amount of newly formed tissue is, with a thickness around 50 μm, approximately the same for all the samples. But at early times, this value is lower with differences between the two samples that had a bioactive coating and those which had not such a coating. Compared to the samples presented in Fig. 7, at 4 weeks the two samples without bioactive coating showed less bone formation. In all the

Table 3
Fitting parameters for the TMS, T-BG and T-BGSr coated systems using the equivalent circuits shown in Fig. 5.

	Rsol (Ω cm^2)	CPEcoat		Rpor (Ω cm^2)	CPEox		Rox (Ω cm^2)	*Ceff* (F cm^{-2})	
		Q (Ω^{-1} cm^{-2} s$^{\alpha}$)	α		Q (Ω^{-1} cm^{-2} s$^{\alpha}$)	α		Mean	SD
TMS									
0	60	1.28E−09	0.96	6.36E+09	–	–	–	6.57E−10	7.06E−11
30	60	9.59E−09	0.81	3.10E+05	1.08E−06	0.70	6.88E+07	5.33E−10	1.98E−11
T-BG									
0	60	2.18E−09	0.95	3.50E+05	1.01E−08	0.60	Inf	9.02E−10	3.97E−11
30	60	2.71E−08	0.75	1.70E+05	9.99E−08	0.71	Inf	3.87E−10	1.37E−10
T-BGSr									
0	60	1.82E−09	0.96	8.57E+05	8.45E−09	0.64	Inf	8.70E−10	6.95E−11
30	60	2.02E−08	0.78	3.06E+04	1.27E−06	0.61	Inf	5.49E−10	1.51E−11

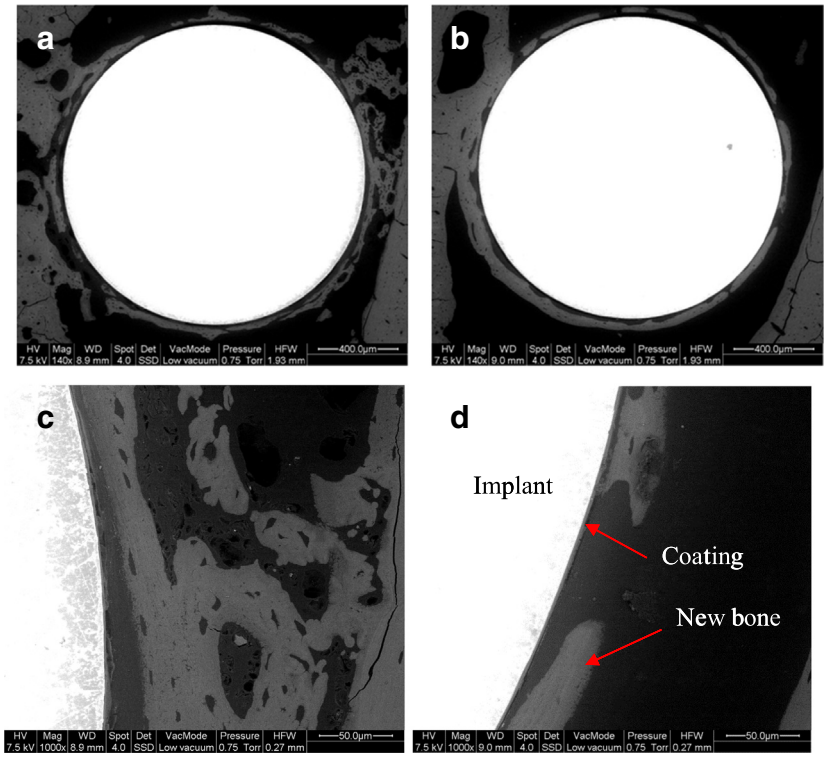

Fig. 7. Back scattering ESEM of a and c (T-BG) and b and d (T-BGSr coated samples) 4 weeks after implantation in rat femur. A detail of the different parts of the system implant/coating/bone was shown with arrows in d.

samples the newly formed bone was not in direct contact with the implant, but a gap of about 10–30 μm was registered. The observation that this gap is biggest in the SS 8 weeks sample fits to previous works [44,45].

The quality of the bone tissue formed around the two different kinds of bioactive coatings, T-BG and T-BGSr, 4 and 8 weeks after implantation in rat femurs, was analyzed via Raman spectroscopy. Fig. 8 shows the Raman spectra in the new bone around the coated T-BG and T-BGSr implants after 4 and 8 weeks of implantation. The difference in the spectra between 4 and 8 weeks is found, in one hand, in the signal intensity and, in the other hand, the presence of new bands in the young bone related to the methacrylate embedding material. This is an indication of the open structure and morphology of the new bone tissue. It is necessary to point out that the youngest tissue of the T-BG was plotted 3 times the real intensity to favor the comparison in the figure.

The analysis of the embedded material was performed by measuring the intensity of the CH_2 wag band (around 1450 cm^{-1}), and the ratio mineral to matrix with PO_4^{3-}/CH_2 wag. In addition, the typical mineral-to-matrix ratio ν_1 PO_4/amide I, the carbonate substitution index (CO_3/ν_1 PO_4) and the degree of crystallinity ($FWMH^{-1}$) were calculated. When comparing T-BG and T-BGSr at early implantation times, the maturity of the tissue formed with strontium particles is clearly seen from the decrease of the methacrylate related bands and the increase of the phosphate ones in the Raman results.

Table 5 summarizes the obtained values of the grid containing 5 × 4 measurement points in each sample. The mineral-to-matrix ratio raised in both coated samples 8 weeks after implantation, as well as the carbonate substitution and crystallinity. The T-BG condition at 4 weeks presents the lowest values and the highest variability errors (around 30%). The other conditions gave error less than 10% for all the parameters studied.

4. Discussion

The hybrid organic–inorganic coating system with bioactive particles has been probed *in vitro* and *in vivo* for corrosion protection and bone regeneration at the implant–tissue interface, showing excellent protective behavior, good *in vitro* response regarding apatite deposition, and promising *in vivo* bone tissue growth. These kinds of coatings on surgical grade stainless steel have probed to create a barrier to media attack and to the release of corrosion products [9,44,46] as well with good tribological stability [12,47,48], therefore making the system metal-coating suitable as long term implant.

In terms of in vivo response, the partial substitution of Ca by Sr ions seems to be supportive in bone regeneration kinetics and tissue quality.

As it was expected, no presence of apatite related compounds were found in the T-BG and T-BGSr samples before immersion, but also no presence of any bands related to the bioactive glass (BG) particles were detected. Obviously only a negligible fraction of particles come out of the coating and most of them close to the surface still remain covered by a thin layer of TMS coating so that they cannot be detected by Raman. The 464 and 790 cm^{-1} bands are from the Si–O–Si vibrational modes, the 600 cm^{-1} is related to the Si–C and the 1274 cm^{-1} is assigned to the $Si–CH_3$ vibration that is present in this kind of systems with thermal treatment temperature below 600 °C [49]. There is also the presence of hydrolysis of methoxy groups with vibrational bands at 665 and 707 cm^{-1} [50].

Table 4
Thickness measurement of the newly formed bone around the implanted samples by analytical calculation of the ESEM images.

Sample	Implantation time (weeks)	New bone thickness (μm)
SS	4	28 ± 13
	8	55 ± 16
TMS	4	23 ± 8
	8	46 ± 12
T-BG	4	35 ± 20
	8	48 ± 8
T-BGSr	4	32 ± 16
	8	52 ± 10

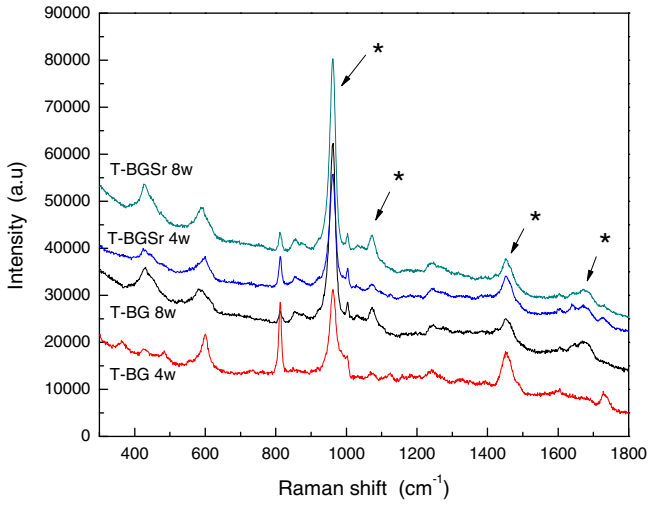

Fig. 8. Raman spectra of the new bone tissue around T-BG and T-BGSr implant 4 and 8 weeks after implantation. The intensity of the T-BG 4 week spectrum was amplified 3 times. Arrows are placed to highlight the bands related to bone quality parameters (*).

After 30 days of immersion, some HA related bands appeared in the T-BG and T-BGSr samples: the typical 960 cm^{-1} band corresponding to PO_4^{3-} first vibration and a PO_4^{3-} third vibration band in 593 cm^{-1} superimposed with the Si–C band. The reaction of the bioactive particles immersed in SBF gave rise to a broad band at 1030–1085 cm^{-1}, which is related to the carbonate, pyrophosphate and phosphate vibration modes of the hydroxyl carbonated apatite (HCA) phase, previous to HA formation [51].

Potentiodynamic and electrochemical impedance spectroscopy tests were carried out for analyzing the integrity of the system before and after immersion in simulated body fluid. After 30 days of immersion the total impedance is still higher than the SS sample for all the cases, but shows a slight decrease for the TMS and the T-BGSr coating systems. This can be attributed to the deterioration of the coatings and to the higher rate of dissolution of the Sr-substituted BG particles when compared with the BG ones [21].

Looking in detail the values of the modeled data of the EIS essays in Tables 2 and 3, it can be noticed that in all coated systems at the beginning of immersion, the value of α for CPEcoat is near 1, indicating that the coating behaves as an ideal capacitor. After the immersion goes on, the layers start to deteriorate, losing the capacity of accumulating charge with high efficiency. It is worth noting, however, that in all the coated systems, with or without bioactive particles, *Ceff* retains a very low value, which indicates – in agreement with the polarization curves – a high integrity of the coatings.

All coated samples, before and after long immersion in SBF, showed a value of *Ceff* of four magnitude orders smaller than the uncoated material ($1.1 \cdot 10^{-5}$ *vs* $4.9 \cdot 10^{-10}$) [52]. The comparison is not strict since the *Ceff* for the TMS, T-BG and T-BGSr systems was calculated with the coating modeled parameters, while for the naked stainless steel the *Ceff* was calculated with the fitted values of the CPEox and Rox for the oxide present in the surface. The low values of the *Ceff* are clearly related to the presence of the protective coating (change of *d* from 5 to 2000 nm) and not being deteriorated with time and/or corrosive attack (*A* is assumed constant in the calculation), since the dielectric constant for iron and chromium oxides (5–13) [53] and for silica based hybrid materials (around 5) [54] do not provide possibilities of change.

When analyzing Rpor, a decrease in the value can be observed for the samples BG and BGSr after 30 days of immersion. This fact could be related to a change in the exposed area of the samples generated by the dissolution of the glass particles that enhances the formation of flaws and defects, showing a slight deterioration of the coatings with time. For the coated samples containing BGSr particles, the estimated resistance is lower than for the coated samples containing BG particles. This could be related to the fact that the Ca ion substitution by Sr ions in the glass network introduces tensions since Sr ions are slightly bigger than the Ca ones. As a result, this distortion increases the rate of dissolution of the BGSr particles compared to the BG ones [55,56] introducing more defects to the coating during dissolution.

From a materials science point of view, the hybrid coatings with bioactive glass and containing Sr-substituted bioactive glass particles presented a good corrosion protection to the aggressive biological media as well as a biological *in vitro* reactivity of the BG and BGSr particles to promote apatite deposition.

The *in vivo* performance is crucial to decide if a biomaterial is suitable for implantation as a prosthetic device. Newman et al. [26] had found that Sr-substituted bioglass has better peri-implant response after 6 weeks of implantation than HAp coated Ti6Al4V implants. In this case, both coatings (T-BG and T-BGSr) presented excellent osseointegration and bone regeneration behavior around the coated materials in a rat model. At an early stage of bone regeneration, as can be seen by ESEM analysis, the thickness of the bone tissue formed around T-BGSr implants is slightly bigger, but not statistically different. But the formed bone seems to be more compact and dense, as can be denoted by the morphological structure and Raman microscopy characterization. In all cases, after 8 weeks, the bone tissue formed around the implants is thicker than at early times. One way to evaluate the effect of the BGSr particles as bone inductive materials is to analyze the quality of the formed bone tissue around the coated bioactive implants by micro Raman spectroscopy and data analysis [37,57–59] evaluating the content of phosphate, relationship between organic matrix and mineral content and beta carbonate substitution. The measurement showed the presence of embedding material (PMMA) in the analyzed bone matrix: the bands observed at 601, 814, 967, 988, 1454 and 1727 cm^{-1} are associated with PMMA [60]. The $\nu 1\ PO_4^{3-}$ at 960 cm^{-1} band, representing the phosphate binding vibrations; the CO_3^{2-} at 1071 cm^{-1}, showing beta-carbonates substitutions; and the amide I at 1643 cm^{-1}, representing the organic collagen part of the bone tissue and 1450 cm^{-1} which is related to the vibrations of the CH_2 side-chain of collagen molecules are used to calculate the ratios $\nu 1\ PO_4$/amide I, $\nu 1\ PO_4/CH_2$ wag and $CO_3/\nu 1\ PO_4$ bands which describe the chemical composition of the bone material (mineral/matrix) [61], of the amount of embedding material present in the sample [62], and the carbonate substitution in order to see the tissue maturity. The mineral to matrix relationship increases 8 weeks after implantation, as well the carbonate substitution and crystallinity in both types of samples. The tissue seems to be mature and stable. But at early implantation times the amount of both collagen matrix and embedding material is larger as determined by the reduction in the $\nu_1 PO_4/CH_2$ wag ratio

Table 5
Results obtained from Raman spectroscopy of the newly formed bone around the T-BG and T-BGSr coated samples 4 and 8 weeks after implantation in the femurs of Wistar rats. The measured values are related to the mineral-to-matrix ratio, aging and crystallinity of the bone (see Materials and methods section).

	T-BG 4 W	T-BG 8 W	T-BG SR 4 W	T-BG SR 8 W
$\nu_1 PO_4$/AMIDE I	5.60 ± 0.44	8.43 ± 0.27	7.94 ± 0.44	10.10 ± 0.41
$\nu_1 CO_3/\nu_1 PO_4$	0.062 ± 0.021	0.1056 ± 0.0041	0.0993 ± 0.0082	0.1245 ± 0.0087
Crystallinity	0.0459 ± 0.0037	0.0523 ± 0.0004	0.0518 ± 0.0009	0.0526 ± 0.0013
$\nu_1 PO_4/CH_2$ WAG	2.015 ± 0.479	5.866 ± 0.437	4.378 ± 0.440	6.048 ± 0.235

than the one present at 8 weeks of implantation. Remarkable is the T-BG sample 4 weeks after implantation showing a high amount of collagen and PMMA in the data collected that can be directly related to the shape and open structure of the newly formed bone in the periphery of the T-BG coated implants. The T-BGSr condition at the same time presents better mineralized characteristics as a mature and stable tissue.

5. Conclusions

Sol gel coatings containing BG and BGSr particles applied onto stainless steel were able to promote apatitic deposition onto their surface when immersed in SBF. Both coatings provide an enhanced corrosion resistance when compared with bare stainless steel in SBF, being a potential film able to provide both corrosion resistance and bioactivity. The in vivo response of the coatings containing Sr-substituted bioglass is better than BG containing coatings at early times of implantation than the one showed at 8 weeks as regards the bone morphology and quality making this functionalized coatings a very promising option for implant protection and bone regeneration.

Acknowledgments

The authors wish to thank to MinCyT/DAAD Cooperation program (project DA11/02) and Agencia de Promoción Científica y Tecnológica (PICT-2010-0917) for the financial support. Also J. Ballarre would like to thank A. Cisilino for the Raman processing analysis.

References

[1] K.S. Katti, Biomaterials in total joint replacement, Colloids Surf., B 39 (2004) 133–142.
[2] I. Milosev, Effect of complexing agents on the electrochemical behavior of orthopaedic stainless steel in physiological solution, J. Appl. Electrochem. 32 (2002) 311–320.
[3] C. Brinker, A.J. Hurd, K.J. Ward, Fundamentals of sol–gel thin film formations, Wiley, New York, 1998.
[4] M. Guglielmi, Rivestimenti sottili mediante dip coating con metodo sol–gel, Rev. Staz. Sper. 4 (1988) 197–199.
[5] C. Sanchez, M. In, Molecular design of alkoxide precursors for the synthesis of hybrid organic–inorganic gels, J. Non-Cryst. Solids 147–148 (1992) 1–12.
[6] N. Pellegri, O. Sanctis, A. Durán, Preparation and microstructure study of borosilicate coatings produced by sol–gel, J. Sol-Gel Sci. Technol. 2 (1994) 519–523.
[7] C.J. Brinker, A.J. Hurd, P.R. Schunk, G.C. Frye, C.S. Ashley, Review of sol–gel thin film formation, J. Non-Cryst. Solids 147–148 (1992) 424–436.
[8] P. Innocenzi, M. Guglielmi, M. Gobbin, P. Colombo, Coating of metals by the sol gel dip-coating method, J. Eur. Ceram. Soc. 10 (1992) 431–436.
[9] A. Durán, A. Conde, A. Gomez Coedo, T. Dorado, C. García, S.M. Ceré, Sol Gel coatings for protective and bioactive functionalisation of metals used in orthopaedic devices, J. Mater. Chem. 14 (2004) 2282.
[10] M. Catauro, F. Bollino, F. Papale, Preparation, characterization, and biological properties of organic–inorganic nanocomposite coatings on titanium substrates prepared by sol–gel, J. Biomed. Mater. Res. Part A 102 (2014) 392–399.
[11] L.L. Hench, J. Wilson, An introduction to bioceramics, in: Hench, Wilson (Eds.), Advanced Series in Ceramics, Vol I, World Scientific, 1993.
[12] J. Ballarre, E. Jimenez-Pique, M. Anglada, S. Pellice, A.L. Cavalieri, Mechanical characterization of nano-reinforced silica based sol–gel hybrid coatings on AISI 316L stainless steel using nanoindentation techniques, Surf. Coat. Technol. 203 (2009) 3325–3331.
[13] T. Kokubo, Design of bioactive bone substitutes based on biomineralization process, Mater. Sci. Eng. C 25 (2005) 97–104.
[14] P. Li, K. de Groot, Calcium phosphate formation within sol–gel prepared titania in vitro and in vivo, J. Biomed. Mater. Res. 27 (1993) 1495–1500.
[15] R.N. Oosterbeek, C.K. Seal, J.M. Seitz, M.M. Hyland, Polymer–bioceramic composite coatings on magnesium for biomaterial applications, Surf. Coat. Technol. 236 (2013) 420–428.
[16] A.A. Gorustovich, T. Steimetz, R.L. Cabrini, J.M. Porto Lopez, Osteoconductivity of strontium-doped bioactive glass particles: a histomorphometric study in rats, J. Biomed. Mater. Res. Part A 92 (2010) 232–237.
[17] H.W. Kim, Y.H. Koh, Y.M. Kong, J.G. Kang, H.E. Kim, Strontium substituted calcium phosphate biphasic ceramics obtained by powder precipitation method, J. Mater. Sci. Mater. Med. 15 (2004) 1129–1134.
[18] S. Panzavolta, P. Torricelli, L. Sturba, B. Bracci, R. Giardino, A. Bigi, Setting properties and in vitro bioactivity of strontium-enriched gelatin-calcium phosphate bone cements, J. Biomed. Mater. Res. A 84 (2007) 965–972.
[19] K. Fujikura, N. Karpukhina, T. Kasuga, D.S. Brauer, R.G. Hill, R.V. Law, Influence of strontium substitution on structure and crystallisation of Bioglass[registered sign] 45S5, J. Mater. Chem. 22 (2012) 7395–7402.
[20] P.J. Marie, Strontium as therapy for osteoporosis, Curr. Opin. Pharmacol. 5 (2005) 633–636.
[21] E. Gentleman, Y.C. Fredholm, G. Jell, N. Lotfibakhshaiesh, M.D. O'Donnell, R.G. Hill, M.M. Stevens, The effects of strontium-substituted bioactive glasses on osteoblasts and osteoclasts in vitro, Biomaterials 31 (2010) 3949–3956.
[22] L.A. Strobel, N. Hild, D. Mohn, W.J. Stark, A. Hoppe, U. Gbureck, R.E. Horch, U. Kneser, A.R. Boccaccini, Novel strontium-doped bioactive glass nanoparticles enhance proliferation and osteogenic differentiation of human bone marrow stromal cells, J. Nanoparticle Res. 15 (2013).
[23] C.T. Wong, Q.Z. Chen, W.W. Lu, J.C. Leong, W.K. Chan, K.M. Cheung, K.D. Luk, Ultrastructural study of mineralization of a strontium-containing hydroxyapatite (Sr-HA) cement in vivo, J. Biomed. Mater. Res. A 70 (2004) 428–435.
[24] G.X. Ni, W.W. Lu, B. Xu, K.Y. Chiu, C. Yang, Z.Y. Li, W.M. Lam, K.D. Luk, Interfacial behaviour of strontium-containing hydroxyapatite cement with cancellous and cortical bone, Biomaterials 27 (2006) 5127–5133.
[25] Y. Li, Q. Li, S. Zhu, E. Luo, J. Li, G. Feng, Y. Liao, J. Hu, The effect of strontium-substituted hydroxyapatite coating on implant fixation in ovariectomized rats, Biomaterials 31 (2010) 9006–9014.
[26] S.D. Newman, N. Lotfibakhshaiesh, M. O'Donnell, X.F. Walboomers, N. Horwood, J.A. Jansen, A.A. Amis, J.P. Cobb, M.M. Stevens, Enhanced osseous implant fixation with strontium-substituted bioactive glass coating, Tissue Eng. Part A 20 (2014) 1850–1857.
[27] A. Awonusi, M.D. Morris, M.M.J. Tecklenburg, Carbonate assignment and calibration in the Raman spectrum of apatite, Calcif. Tissue Int. 81 (2007) 46–52.
[28] M.D. O'Donnell, P.L. Candarlioglu, C.A. Miller, E. Gentleman, M.M. Stevens, Materials characterisation and cytotoxic assessment of strontium-substituted bioactive glasses for bone regeneration, J. Mater. Chem. 20 (2010) 8934–8941.
[29] Z. Jingxian, J. Dongliang, L. Weisensel, P. Greil, Deflocculants for tape casting of TiO_2 slurries, J. Eur. Ceram. Soc. 24 (2004) 2259–2265.
[30] T. Kokubo, H. Kushitani, S. Sakka, T. Kitsugi, T. Yamamuro, Solutions able to produce in vivo surface–structure changes in bioactive glass–ceramic A–W, J. Biomed. Mater. Res. 24 (1990) 721–734.
[31] Zplot for Windows, Electrochem. Impedance Software Operating Manual, Part 1, Scribner Ass. Inc., Southern Pines, NC, 1998.
[32] C.H. Hsu, F. Mansfeld, Technical note: concerning the conversion of the constant phase element parameter Y0 into a capacitance, Corrosion NACE 57 (2001) 747–748.
[33] J.B. Jorcin, M.E. Orazem, N. Pébère, B. Tribollet, CPE analysis by local electrochemical impedance spectroscopy, Electrochim. Acta 51 (2006) 1473–1479.
[34] B. Hirschorn, M.E. Orazem, B. Tribollet, V. Vivier, I. Frateur, M. Musiani, Determination of effective capacitance and film thickness from constant-phase-element parameters, Electrochim. Acta 55 (2010) 6218–6227.
[35] G.J. Brug, A.L.G. Van Den Eeden, M. Sluyters-Rehbach, J.H. Sluyters, The analysis of electrode impedances complicated by the presence of a constant phase element, J. Electroanal. Chem. 176 (1984) 275–295.
[36] T.E. Oliphant, Python for scientific computing, Comput. Sci. Eng. 9 (2007) 10–20.
[37] J. Ballarre, P.M. Desimone, M. Chorro, M. Baca, J.C. Orellano, S.M. Ceré, Bone quality around bioactive silica-based coated stainless steel implants: analysis by Micro-Raman, XRF and XAS techniques, J. Struct. Biol. 184 (2013) 164–172.
[38] R.M. Hoerth, M.R. Katunar, A. Gomez Sanchez, J.C. Orellano, S.M. Ceré, W. Wagermaier, J. Ballarre, A comparative study of zirconium and titanium implants in rat: osseointegration and bone material quality, J. Mater. Sci. Mater. Med. 25 (2014) 411–422.
[39] J.S. Yerramshetty, O. Akkus, The associations between mineral crystallinity and the mechanical properties of human cortical bone, Bone 42 (2008) 476–482.
[40] A. Carden, M.D. Morris, Application of vibrational spectroscopy to the study of mineralized tissues (review), J. Biomed. Opt. 5 (2000) 259–268.
[41] M.B. González, S.B. Saidman, Electrodeposition of bilayered polypyrrole on 316L stainless steel for corrosion prevention, Prog. Org. Coat. 78 (2015) 21–27.
[42] A. Duran, A. Conde, A. Gómez Coedo, T. Dorado, C. García, S. Ceré, Sol–gel coatings for protection and bioactivation of metals used in orthopaedic devices, J. Mater. Chem. 14 (2004) 2282–2290.
[43] M.E. Orazem, B. Tribollet, Equivalent circuits analogs, Electrochemical Impedance Spectroscopy, Wiley, New Jersey, US, 2008. 157–158.
[44] J. Ballarre, Y. Liu, E. Mendoza, H. Schell, F. Díaz, J.C. Orellano, P. Fratzl, C. García, S.M. Ceré, Enhancing low cost stainless steel implants: bioactive silica-based sol–gel coatings with wollastonite particles, Int. J. Nano Biomater. 4 (2012) 33–53.
[45] J. Ballarre, I. Manjubala, W.H. Schreiner, J.C. Orellano, P. Fratzl, S. Ceré, Improving the osteointegration and bone–implant interface by incorporation of bioactive particles in sol–gel coatings of stainless steel implants, Acta Biomater. 6 (2010) 1601–1609.
[46] J. Ballarre, D.A. López, W.H. Schreiner, A. Durán, S.M. Ceré, Protective hybrid sol–gel coatings containing bioactive particles on surgical grade stainless steel: surface characterization, Appl. Surf. Sci. 253 (2007) 7260–7264.
[47] J. Ballarre, D.A. López, A.L. Cavalieri, Nano-indentation of hybrid silica coatings on surgical grade stainless steel, Thin Solid Films 516 (2008) 1082–1087.
[48] J. Ballarre, D.A. López, A.L. Cavalieri, Frictional and adhesive behavior of organic–inorganic hybrid coatings on surgical grade stainless steel using nano-scratching technique, Wear 266 (2009) 1165–1170.
[49] J. Yang, J. Chen, J. Song, Studies of the surface wettability and hydrothermal stability of methyl-modified silica films by FT-IR and Raman spectra, Vib. Spectrosc. 50 (2009) 178–184.
[50] A. Depla, E. Verheyen, A. Veyfeyken, M. Van Houteghem, K. Houthoofd, V. Van Speybroeck, M. Waroquier, C.E.A. Kirschhock, J.A. Martens, UV-Raman and ^{29}Si NMR spectroscopy investigation of the nature of silicate oligomers formed by acid catalyzed hydrolysis and polycondensation of tetramethylorthosilicate, J. Phys. Chem. C 115 (2011) 11077–11088.

[51] M. Cerruti, C.L. Bianchi, F. Bonino, A. Damin, A. Perardi, C. Morterra, Surface modifications of bioglass immersed in TRIS-buffered solution. A multitechnical spectroscopic study, J. Phys. Chem. B 109 (2005) 14496–14505.
[52] P.H. Suegama, H.G. de Melo, A.A.C. Recco, A.P. Tshiptschin, I.V. Aoki, Corrosion behavior of carbon steel protected with single and bi-layer of silane films filled with silica nanoparticles, Surf. Coat. Technol. 202 (2008) 2850–2858.
[53] Y. Tanaka, H. Saito, Y. Tsutsumi, H. Doi, H. Imai, T. Hanawa, Active hydroxyl groups on surface oxide film of titanium, 316L stainless steel, and cobalt–chromium–molybdenum alloy and its effect on the immobilization of polyethylene glycol, Mater. Trans. 49 (2008) 805–811.
[54] C.S. Kim, H.D. Jeong, What originates the dielectric permittivity of silicate-silsesquioxane hybrid thin films? J. Phys. Chem. B 112 (2008) 16257–16260.
[55] M.D. O'Donnell, Y. Fredholm, A. de Rouffignac, R.G. Hill, Structural analysis of a series of strontium-substituted apatites, Acta Biomater. 4 (2008) 1455–1464.
[56] M.D. O'Donnell, R.G. Hill, Influence of strontium and the importance of glass chemistry and structure when designing bioactive glasses for bone regeneration, Acta Biomater. 6 (2010) 2382–2385.
[57] X. Bi, C.A. Patil, C.C. Lynch, G.M. Pharr, A. Mahadevan-Jansen, J.S. Nyman, Raman and mechanical properties correlate at whole bone- and tissue-levels in a genetic mouse model, J. Biomech. 44 (2011) 297–303.
[58] S. Gamsjaeger, A. Masic, P. Roschger, M. Kazanci, J.W.C. Dunlop, K. Klaushofer, E.P. Paschalis, P. Fratzl, Cortical bone composition and orientation as a function of animal and tissue age in mice by Raman spectroscopy, Bone 47 (2010) 392–399.
[59] M. Kazanci, P. Roschger, E.P. Paschalis, K. Klaushofer, P. Fratzl, Bone osteonal tissues by Raman spectral mapping: orientation–composition, J. Struct. Biol. 156 (2006) 489–496.
[60] A. Matsushita, Y. Ren, K. Matsukawa, H. Inoue, Y. Minami, I. Noda, Y. Ozaki, Two-dimensional Fourier-transform Raman and near-infrared correlation spectroscopy studies of poly(methyl methacrylate) blends. 1. Immiscible blends of poly(methyl methacrylate) and atactic polystyrene, Vib. Spectrosc. 24 (2000) 171–180.
[61] M.D. Morris, G.S. Mandair, Raman assessment of bone quality, Clin. Orthop. Relat. Res. 469 (2011) 2160–2169.
[62] Y.N. Yeni, J. Yerramshetty, O. Akkus, C. Pechey, C.M. Les, Effect of fixation and embedding on Raman spectroscopic analysis of bone tissue, Calcif. Tissue Int. 78 (2006) 363–371.